Spatial Phase Distributions in Solution-Based and Evaporated Cs-Pb-Br Thin Films

Sebastian Caicedo-Davila[1‡], Hannah Funk[1‡], Robert Lovrinčić[2], Christian Müller[2], Michael Sendner[3], Oana Cojocaru-Mirédin[4], Frederike Lehmann[1], René Gunder[1], Alexandra Franz[1], Ayala V. Cohen[5] , Leeor Kronik[5], Benedikt Haas[6], Christoph T. Koch[6], Sergej Levcenco[1], Daniel Abou-Ras[1]*

[1] Helmholtz-Zentrum Berlin für Materialien und Energie GmbH, Hahn-Meitner-Platz 1, 14109 Berlin, Germany.

[2] InnovationLab GmbH, Speyerer Straße 4, 69115 Heidelberg, Germany.

[3] Kirchhoff Institute for Physics, Heidelberg University, Im Neuenheimer Feld 227, 69120 Heidelberg, Germany.

[4] Institute of Physics, RTWH Aachen University, Sommerfelderstr. 14, 52074 Aachen, Germany

[5] Department of Materials and Interfaces, Weizmann Institute of Science, Rehovoth 76100, Israel.

[6] Humboldt-Universität zu Berlin, Institut für Physik, Newtonstraße 15, 12489 Berlin, Germany.

Abstract

In recent years, inorganic cesium-lead-halide perovskites, $CsPbX_3$ (X=I, Br, Cl), have attracted

interest for optoelectronic applications such as highly efficient thin-film light-emitting diodes or wide-gap absorber materials for photovoltaics. However, phase segregation and secondary phases in as-deposited thin films are still considered to be limiting factors for devices based on $CsPbX_3$. Here, we report a correlative electron microscopy and spectroscopy approach for the identification of secondary phases and their distributions in Cs-Pb-Br thin films, deposited by solution-based and coevaporation methods on various substrates. We identified phases by their compositional, structural, and optoelectronic properties, using X-ray diffraction, spectroscopy and a variety of microscopy techniques. We found that the Cs-Pb-Br films contain ternary Cs_4PbBr_6 and $CsPb_2Br_5$ phases in addition to $CsPbBr_3$, a finding consistent with calculations of formation enthalpies by means of density functional theory showing that these values are very similar for the three ternary phases. We find that these phases can exhibit different spatial distributions inside the film and discuss the influence of the deposition method and synthesis parameters on the resulting phase composition of the Cs-Pb-Br layers.

1. Introduction

With increasing power conversion efficiencies surpassing 22% in 2018[1] and low-processing costs, hybrid organic-inorganic lead-halide perovskites attract ever more interest in the photovoltaics community.[2,3] In spite of this extraordinary progress in device performance stability and band-gap tuning still remain limiting factors – on top of the toxicity of lead – holding back the commercialization of perovskite-based devices.[2,4] The inorganic cesium-lead-bromide perovskite, $CsPbBr_3$, has been investigated as a wide-gap absorber for photovoltaics, as its performance is comparable to the organic bromide variants, with added enhanced stability .[5,6] Inorganic perovskites are also attractive for other optoelectronic applications, e.g., as an active material for light emitting diodes.[7–9] While phase formation in large $CsPbBr_3$ crystals and nanostructures has been investigated,[10–12] we are not aware of any study on the spatial distribution of secondary phases

in polycrystalline CsPbBr$_3$ thin-films, including consequences for the optoelectronic properties on a macroscopic scale.

In the present work, we correlate X-ray diffraction (XRD) and a variety of microscopy techniques to investigate the structural, compositional, and optoelectronic properties of Cs-Pb-Br thin films, with an emphasis on the spatial phase distribution at a micro- and nanoscopic level. We compare thin films synthesized by one- and two-step solution-based processes, as well as by coevaporation, and find that thin films with an intended stoichiometry of CsPbBr$_3$ are actually composed of various Cs-Pb-Br phases. Density functional theory (DFT) calculations of the formation enthalpies of these phases show that their values are very similar. Therefore, a Cs-Pb-Br thin film is always likely to contain more than one Cs-Pb-Br phase. Furthermore, the phase distributions detected for the analyzed Cs-Pb-Br systems may be substantially different in films for which the deposition recipes have been only slightly changed.

2. Structural properties of binary and ternary compounds in the Cs-Pb-Br phase diagram

The structure of CsPbBr$_3$ has been studied since the 1950s,[13,14] to determine its temperature-dependent phase transitions, but also to investigate the ternary compositional phase diagram of Cs-Pb-Br. CsPbBr$_3$ undergoes two crystal phase transitions upon cooling, from cubic (*Pm3m*, No. 221) to tetragonal (*P4/mbm*, No. 127) at 130 °C, and to orthorhombic (*Pbnm*, No. 62) at 88 °C,[10,15] making the latter space group the relevant one at room temperature and for solar-cell operation conditions.[16] The cubic phase exhibits a perovskite structure, while the orthorhombic phase needs four times the number of atoms to correctly describe the unit cell,[14] owing to the tilting of the PbBr$_6$ octahedra (see **Figure 1**b).[10] Some of the older structural studies refer to the room temperature phase of CsPbBr$_3$ as monoclinic[13,14,17–19] whereas other studies, including more recent ones, consider an orthorhombic crystal structure.[10,15,20,21]

3
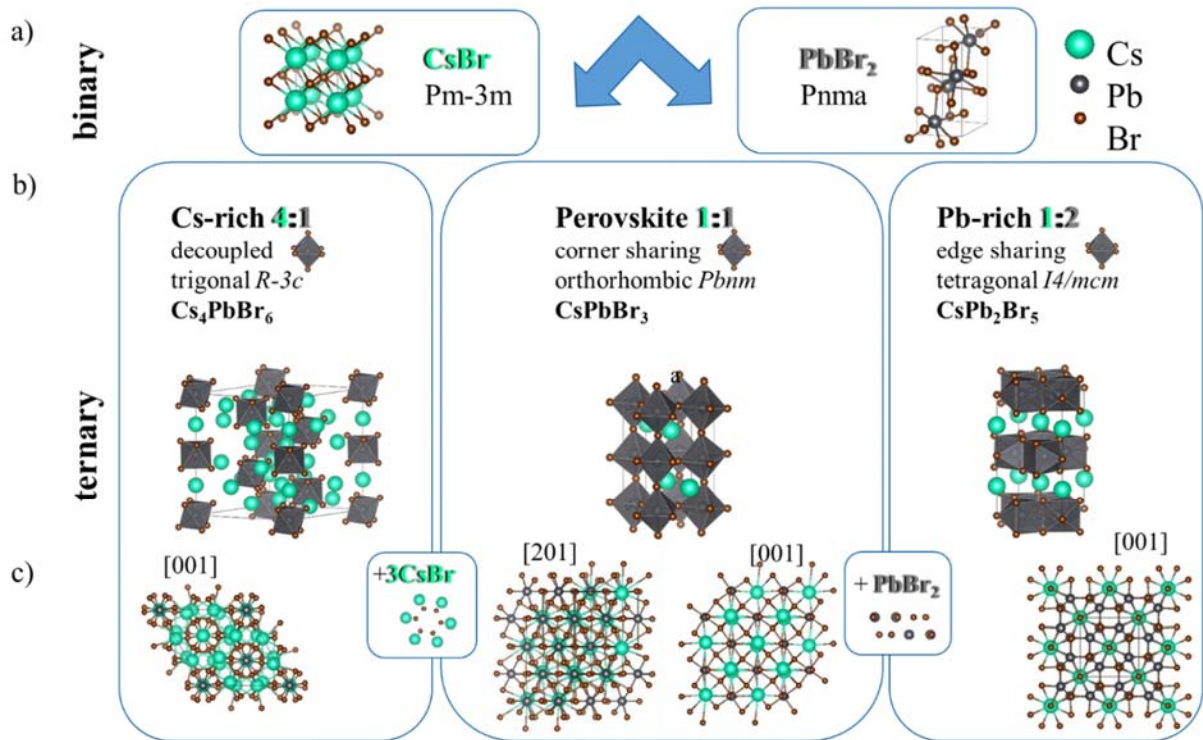
Figure 1. Binary and ternary components of the ternary phase diagram of Cs-Pb-Br at room temperature, viewed from different directions

The lattice parameters of orthorhombic and monoclinic phases are quite similar, with monoclinic descriptions reporting γ angles of 89.65°[14] or 89.39°[17] and hence deviating only slightly from an orthorhombic crystal structure. The ternary phase diagram of Cs-Pb-Br shows that not only $CsPbBr_3$, but also $CsPb_2Br_5$ and Cs_4PbBr_6 are stable phases that can be grown reproducibly, using different ratios of CsBr and $PbBr_2$ with similar synthesis conditions.[17,22] The crystal structures of the two binary precursors and the three ternary Cs-Pb-Br phases at room temperature are presented in Figure 1. A ratio of 4:1 [Cs]/[Pb] yields the Cs-rich Cs_4PbBr_6 phase (*R-3c*, No. 167)[23], a ratio of 1:1 yields the perovskite $CsPbBr_3$ phase, and a ratio of 1:2 yields the Pb-rich $CsPb_2Br_5$ (*I4/mcm*, No. 140)[17] phase. Figure 1c additionally illustrates the different ternary phases from various viewing directions. For example, $CsPbBr_3$ viewed from the [201] direction resembles Cs_4PbBr_6 viewed from the [001] direction, as well as $CsPb_2Br_5$ viewed from the [001] direction. The structural similarities are reflected in similar peak positions in diffraction experiments, presented

below (Section 4.1).

3. Materials and Methods

3.1 Sample Preparation

3.1.1 Single-step, spin-coated films on glass

One-step solution processed films were prepared by spin coating in a nitrogen atmosphere. 0.8 M of $PbBr_2$ and CsBr in dimethyl sulfoxide (DMSO) were spin-coated on preheated (75 °C) substrates. During the third spin step, 2-propanol was dropped on the spinning substrate. It was then dried on a hot plate at 70 °C for 15 min.

3.1.2 Two-step, spin-coated films on glass

Two-step solution processed films were fabricated according to a previously published method.[5] In brief, 1 M $PbBr_2$ in dimethylformamide (DMF) was spin-coated on a pre-heated (75 °C) substrate. The $PbBr_2$ films were subsequently dipped for 10 min in a CsBr solution in methanol. All steps were carried out in nitrogen atmosphere.

3.1.3 Co-evaporated films

Substrates were loaded in a high-vacuum chamber with a base pressure of $\sim10^{-7}$ mbar. $PbBr_2$ and CsBr were thermally evaporated while the respective rates were monitored with two quartz microbalances. The resulting films were subsequently annealed in nitrogen at 100 °C for 15 min.

3.1.4 CsPbBr3 powder sample

$CsPbBr_3$ was synthesized from an equimolar mixture of CsBr (99.99% from Ossila) and $PbBr_2$ (98+%, extra pure, from Arcos Organics) in DMF (99,8 %, Roth) and left to stir overnight at 60 °C, followed by evaporation of the solvent at 85 °C and annealing at 140 °C for 1 h. The samples were stored under N_2 to avoid potential degradation by oxygen and humidity.

3.2 Structural characterization

XRD patterns were acquired by means of a PANalytical X'Pert MPD Pro X-ray diffractometer at room temperature, in a Bragg-Brentano configuration, using a Cu K-α radiation source (λ =0.15406 nm). Bright-field transmission electron microscope (TEM) images and electron diffraction (ED) patterns were acquired using a Zeiss Libra 200 TEM operating at 200 kV. To prevent sample degradation, a very low dose method was chosen to gather structural information from a large area of the film. With a condenser aperture limiting the illuminated area to a diameter of 305 ± 5, nm an automated script was used to acquire 15×15 energy filtered ED patterns with acquisition times of 1 s per frame and a spatial increment of 0.2 µm. This resulted in structural information from an area of 10.89 µm^2, while keeping the dose rate as low as 10^{16} electrons cm^{-2}. A thallium chloride reference was used for camera length calibration. The 225 diffraction patterns were superimposed and the intensity profiles evaluated with an azimuthal integration with the ProcessDiffraction Software.[24]

3.3 Topography and compositional mapping

Atomic force microscope (AFM) images were acquired using a Smart SPM-1000 from AIST-NT. The measurements were performed in tapping mode using polysilicon cantilever from TipsNano (reference HA FM/WC), with a nominal resonance frequency of 380 kHz and a spring constant of 34 N m^{-1}. Images were treated with average plane flattening and all the processing and data extraction were carried out using the Gwyddion software.[25]

Energy-dispersive X-ray spectrometry (EDX) maps were acquired by means of an Oxford Instruments XMax80 X-ray detector in a Zeiss UltraPlus scanning electron microscope (SEM). Measurements were performed at an acceleration voltage of 10 kV and a beam current of about 1 nA. For quantification of stoichiometry, Cs-L, Pb-M and Br-L X-ray characteristic lines were used.

Atom probe tomography (APT) measurements were carried out by CAMECA LEAP 4000X Si instrument with laser pulses of 355 nm wavelength (UV), 10 ps pulse length, and 2 pJ pulse energy. The specimen base temperature was set to 50 K. APT samples (shown in Figure S7) were prepared using focused ion beam (FIB) milling as described in ref. 26. To minimize beam damage, a low energy (2 keV) Ga beam was used at the final ion-milling stage.

3.4 Luminescence mapping

Cathodoluminescence (CL) hyperspectral maps were acquired by means of a Zeiss MERLIN SEM using a SPARC system from Delmic, equipped with a Kymera 193i spectrograph and a Zyla 5.5 sCMOS camera from Andor. A monochromator grating of 300 lines mm^{-1} blazed at 500 nm was used. The exposure time was varied between 20 and 100 ms to ensure a good signal-to-noise ratio, while avoiding saturation; the exact value of the integration time for each sample is described below (Section 4). The acceleration voltage was set to 8 kV and the current on the sample surface was 200 pA for the single-step, spin-coated film (described in Section 4.1.1), and 900 pA for the the rest of the films. All the CL spectra presented were treated by background (beam-blanked acquisition) subtraction and compensation using the spectrometer transfer function. The CL hyperspectral maps measured with a magnification lower than 5000 exhibit an instrumental error in alignment. The gradient in the measured wavelengths was subtracted from the reported CL emission peak maps.

Photoluminescence (PL) spectra were dispersed by a 1/2 m grating monochromator coupled with CCD detector. The investigated samples were excited with a 409 nm diode laser (a spot radius of ∼100 μm and an excitation intensity in the range of 0.3- 1.9 W cm^{-2}).

3.5 DFT calculations of formation enthalpies

All DFT calculations of the formation enthalpies were performed using the Perdew-Burke-Ernzerhof (PBE)[27] form of the generalized-gradient approximation, augmented by dispersion terms

calculated within the Tkatchenko-Scheffler scheme[28] using an iterative Hirshfeld partitioning of the self-consistently computed charge density, which is highly useful for describing ionic compounds with components of dispersive binding.[29,30] All calculations were performed using the Vienna ab initio simulation package (VASP),[31] a plane-wave basis code in which ionic cores are described by the projected augmented wave (PAW)[32] method. A 10^{-6} eV convergence criterion for the total energy was used in all calculations, and the forces acting on the ions were relaxed to below 10^{-2} eV Å^{-1}. Plane-wave cutoffs of 600, 800, and 300 eV were used for all ternary phases, the PbBr$_2$ phase, and the CsBr phase, respectively. A $3 \times 3 \times 3$ k-point grid was utilized for sampling the Brillouin zone of the Cs$_4$PbBr$_6$ phase, a $4 \times 4 \times 4$ grid was used for the CsPb$_2$Br$_5$ phase, a $5 \times 5 \times 5$ grid for the CsPbBr$_3$ and CsBr phases, and a $6 \times 7 \times 6$ grid for the PbBr$_2$ phase. Convergence was tested for all of the above parameters. Relaxation of the ternary phases was performed using the GADGET optimizer.[33] Additional tests, in which spin-orbit coupling was included and the volume was allowed to relax, showed no meaningful changes in the results.

4. Results

In this section, we first provide an overview of the phases contained in our Cs-Pb-Br thin films, based on the integral XRD analysis given in subsection 4.1. Next, in subsection 4.2 we show the results of DFT calculations for the formation enthalpies of the binary and ternary phases. Finally, we present our findings of the spatial phase distributions obtained from EDX and CL correlative microscopy on various Cs-Pb-Br thin films and discuss them in relation to the XRD and DFT results (Section 4.3 to 4.6).

4.1 Crystal structures detected in Cs-Pb-Br films deposited by various techniques

Figure 2a to d shows XRD patterns from all our Cs-Pb-Br thin films, in comparison with that of a CsPbBr$_3$ powder reference (Figure 2e). In addition to peaks similar to those of the orthorhombic

CsPbBr$_3$ phase of the reference, the XRD patterns obtained from the thin films exhibit additional peaks that according to literature can be assigned to secondary phases (Cs$_4$PbBr$_6$ PDF 01-077-8224,[23] CsPbBr$_3$ PDF 01-072-7929,[15] CsPb$_2$Br$_5$ PDF 00-025-0211[17], PbBr$_2$ COD 1530324,[34] and CsBr COD ID 9008788[35]). Correspondingly, the single-step solution-processed film (Figure 2a) consists of CsPbBr$_3$ and Cs$_4$PbBr$_6$, while the two-step solution-processed film (Figure 2b) contains CsPbBr$_3$, CsPb$_2$Br$_5$, and CsBr.
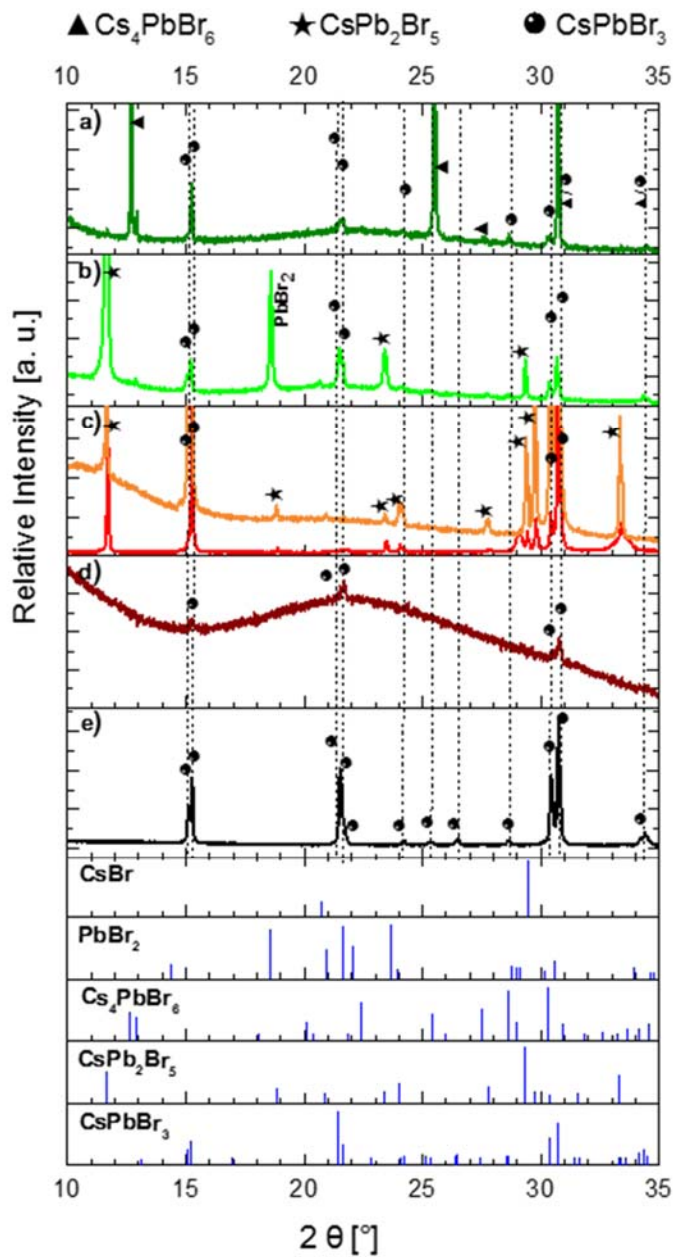
Figure 2. X-ray diffractogram of (a) single-step solution processed, (b) two-step solution processed, (c) coevaporated 700 nm (orange: on glass; red: on Si), (d) coevaporated 70 nm on a carbon coated Cu-Grid films, and (e) powder. For indexing of the XRD patterns we refer to Cs_4PbBr_6 PDF 01-077-8224,[23] $CsPbBr_3$ PDF 01-072-7929[15], $CsPb_2Br_5$ PDF 00-025-0211[17], $PbBr_2$ COD 1530324,[34] and $CsBr$ COD ID 9008788.[35]

The diffractogram of the 700 nm thick coevaporated films (Figure 2c) confirms the secondary

phase to be $CsPb_2Br_5$. Peaks attributed to $CsPbBr_3$ were also measured. However, the 112, 020 and

002 peaks around $2\theta = 21.55 \pm 0.09°$, corresponding to a lattice spacing of about 0.41 nm are not present. These peaks are also weak in the XRD pattern of the single-step, solution-processed film, with similar diffractograms reported in the literature,[36] which may be attributed to preferred orientation of the film.

It is interesting that the XRD pattern of the 70 nm thin film, which was coevaporated on a carbon-coated Cu grid (Figure 2d) exhibits all the major peaks of the reference (Figure 2e). However, the poor statistics – due to the small excitation volume – do not allow an unambiguous determination of the crystal structure of the film. Further insight will be provided by using ED for a high-resolution, structural characterization of this Cs-Pb-Br film further below (Section 4.6).

4.2 Calculated formation enthalpies of the Cs-Pb-Br ternary phases

All DFT-calculated formation enthalpies for different Cs-Pb-Br reactions were calculated using:

$$\Delta H = \sum E_{tot}(products) - \sum E_{tot}(reactants),$$

where $E_{tot}(X)$ is the total energy per formula unit of phase X.

The results are summarized in **Table 1**. All reactions were found to have a negative formation enthalpy, indicating the stability of the phases. Out of the three ternary phases, Cs_4PbBr_6 is the most stable, followed by $CsPb_2Br_5$ and $CsPbBr_3$. These results are in good agreement with the recently published work of Yin et al.,[37] further supporting their validity.

Table 1: Formation enthalpies per formula unit of the Cs-Pb-Br ternary phases from DFT calculations. A full list of the formation enthalpies for additional reactions is given in the supporting information.

#	Reaction	Formation enthalpy [eV]
1	$PbBr_2 + CsBr \iff CsPbBr_3$	-0.26
2	$PbBr_2 + 4CsBr \iff Cs_4PbBr_6$	-0.53

| 3 | $2PbBr_2 + CsBr \iff CsPb_2Br_5$ | -0.35 |

4.3 Single-step, spin-coated films on glass

Figure 3a and b show SEM images from the surface and cross-section of a single-step, spin-coated Cs-Pb-Br film, which is composed of a porous matrix with precipitates embedded in it. AFM topography (Figure 3c and d) reveals that the precipitates are almost three times thicker than the matrix film. They exhibit an average thickness of about 700-750 nm, while the matrix is only 250-300 nm thick.
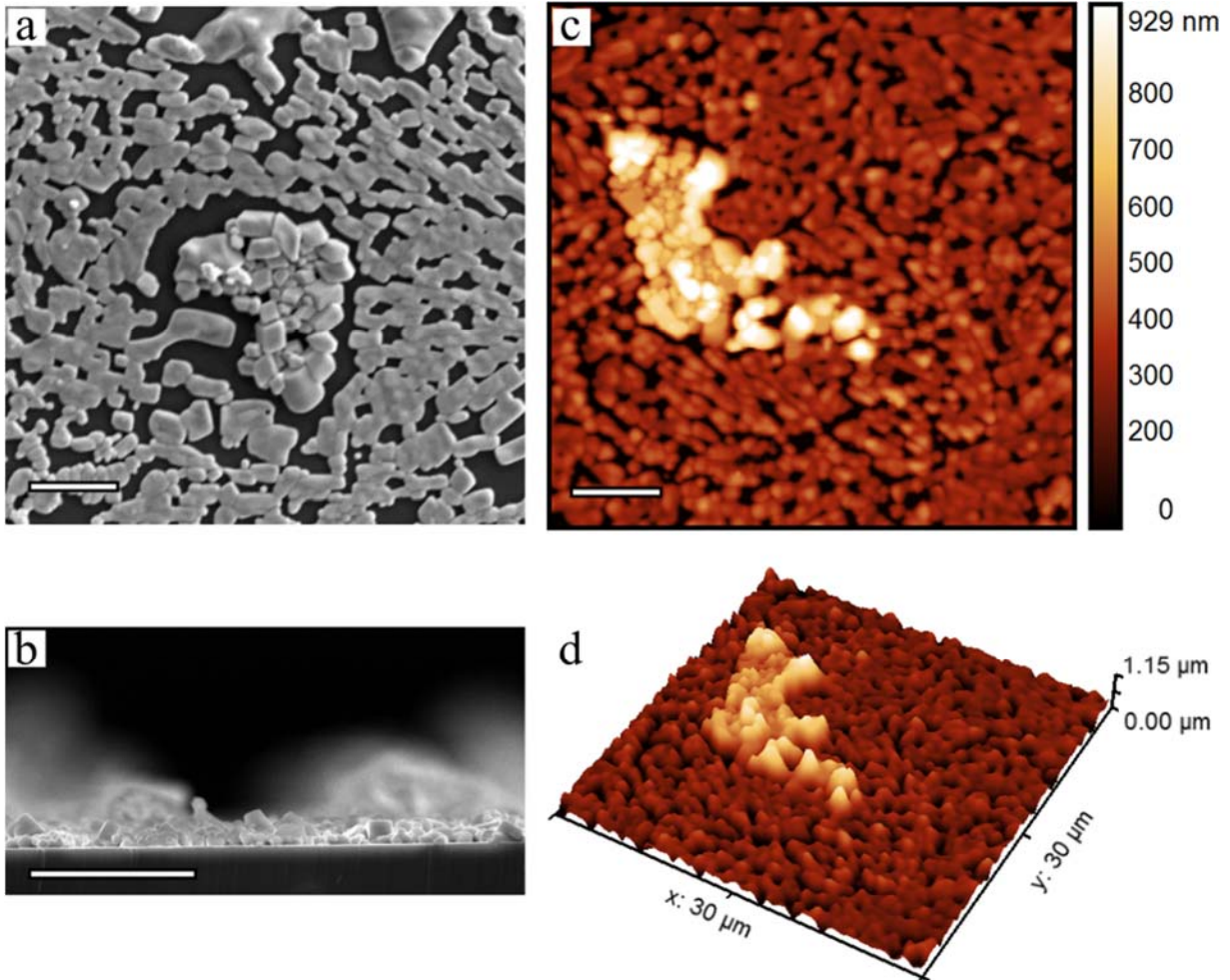
Figure 3. Morphology of a Cs-Pb-Br film, spin-coated on a glass substrate using the single-step synthesis method: SEM images of the (a) surface and (b) cross-section, and AFM (c) image and (d) 3D topography. Note that the precipitates are almost three times thicker than the matrix film.

All scale bars are 5 μm.

In order to investigate these different regions, we performed CL and EDX measurements on the same area, using a correlative microscopy approach.[38,39] The CL maps are given in **Figure 4**a and b, showing that the matrix film is highly luminescent, while the precipitates are dark in the probed spectral range, between 1.7 and 2.6 eV. The CL intensity of the matrix film is non-uniform, with observed regions of high intensity around the precipitates. The radiative transition at 2.35 eV (see the accumulated CL spectrum in Figure 4c) exhibits negligible position variations over the matrix film and is in good agreement with the value reported in the literature for bulk $CsPbBr_3$,[5,40–43] thus confirming the XRD result.
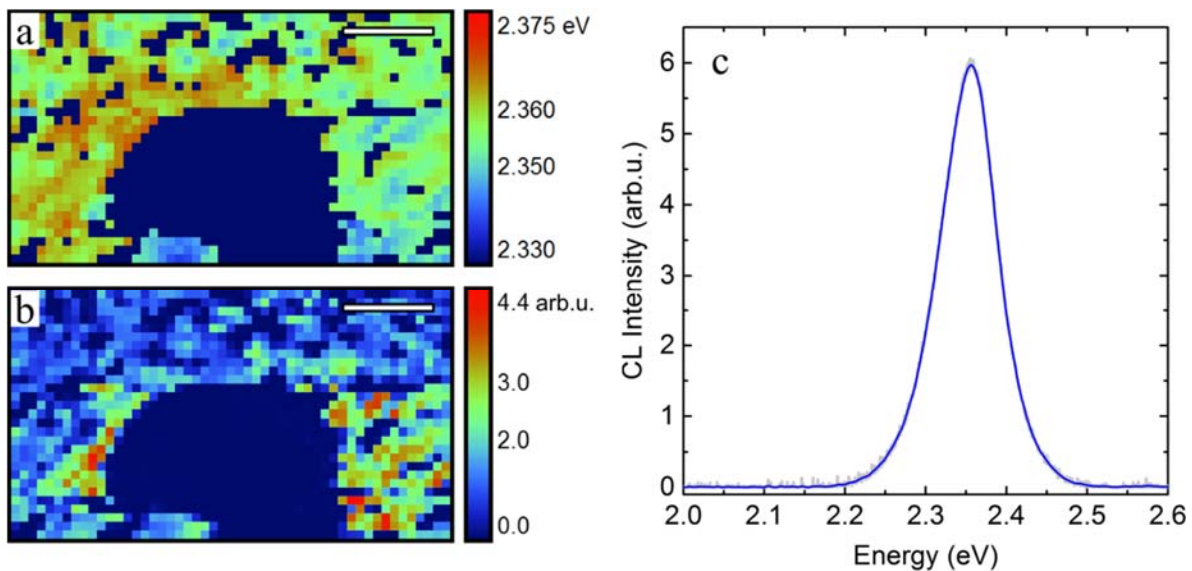
Figure 4. Optical properties of a Cs-Pb-Br film spin-coated on glass shown in Figure 3: (a) map of the emission peak, (b) CL intensity map and (c) accumulated CL spectrum. The precipitates show no measurable CL response, whereas the intensity is stronger on the matrix film surrounding them. Note that the CL peak position on the matrix film remains constant. All scale bars are 5 μm and the used exposure time for the CL measurements was 50 ms.

We measured different compositions for the matrix and precipitates using EDX, as shown in **Figure 5e**. The EDX linescan extracted across a precipitate shows enhanced Cs and reduced Pb signals in the precipitates, with respect to the matrix film, while the Br signal count remains constant. Since EDX quantification requires delicate calibration to report an accurate

13

stoichiometry, we report the relative increase in the net counts averaged at the different phases (see Table S1): the difference in the Br counts between the matrix and the precipitates is negligible. However, Pb counts reduce to half in the precipitates and the Cs counts almost double. The composition of the precipitates – relative to the $CsPbBr_3$ luminescent matrix – is approximately $Cs_2Pb_{0.5}Br_3$, matching the stoichiometry of the Cs_4PbBr_6 phase.
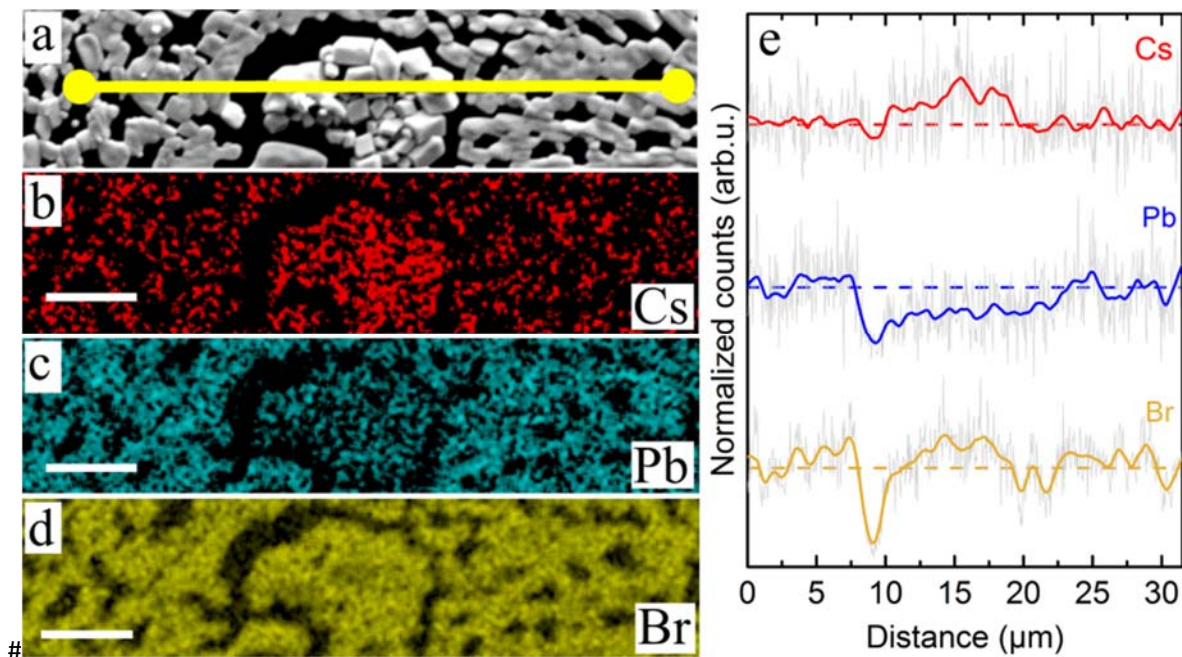

Figure 5. Composition of a Cs-Pb-Br film spin-coated on glass, shown in Figure 3: (a) SEM image showing the path used to obtain the EDX linescan in (e), and the corresponding compositional maps, showing the distribution of (b) Cs, (c) Pb and (d) Br. The precipitates exhibit an increase in Cs and a depletion of Pb, compared with the matrix film, while Br remains constant. All scale bars are 5 μm.

The optical properties of this phase are currently a matter of debate. Mohamed et al. and others have published data showing high luminescence of Cs_4PbBr_6[44–48] and attributed the green emission to intrinsic, deep, mid-gap traps and quantum-size emission sites.[37,48–50] Several other authors reported that Cs_4PbBr_6 exhibits a large band-gap energy (~ 4.0 eV), and assigned the green emission to inclusions and hybridization with the perovskite phase $CsPbBr_3$.[51–55] Calculations by Jung et al. confirmed the possible coexistence of $CsPbBr_3$ and Cs_4PbBr_6 due to the narrow stability field of Cs_4PbBr_6 in chemical potential space,[56] and those by Kang and Han indicate that the

14

embedded $CsPbBr_3$ nanostructures are responsible of the green luminescence in Cs_4PbBr_6.[57,58] In addition, a very recent paper on CL and EDX characterization of Cs_4PbBr_6 powders, convincingly shows that the green luminescence originates at embedded $CsPbBr_3$ nanocrystals.[59] Our correlative analysis, which includes composition, structure, and optical properties, provides sufficient evidence to conclude that the precipitate phase is in fact non-luminescent Cs_4PbBr_6.

4.4   Two-step, solution-based films on glass

The topography of the two-step, solution-processed film, deposited on glass is different from that of the single-step, spin-coated film, featuring a small-grain, closed film with precipitates deposited on top of it. These "islands" are micrometer sized, and in contrast with the precipitates in the single-step, spin-coated film, they are not formed by crystallites, but show a rather "cauliflower" shape (**Figure 6**a). The high contrast between the islands and the film in the in-lens detector image (Figure S1) suggests that they are different materials. The EDX map of the surface, along with the linescan extracted from it (Figure 6b to f), shows a similar case as for the single-step film: depletion of the Pb and enhancement of the Cs counts, while Br remains constant.
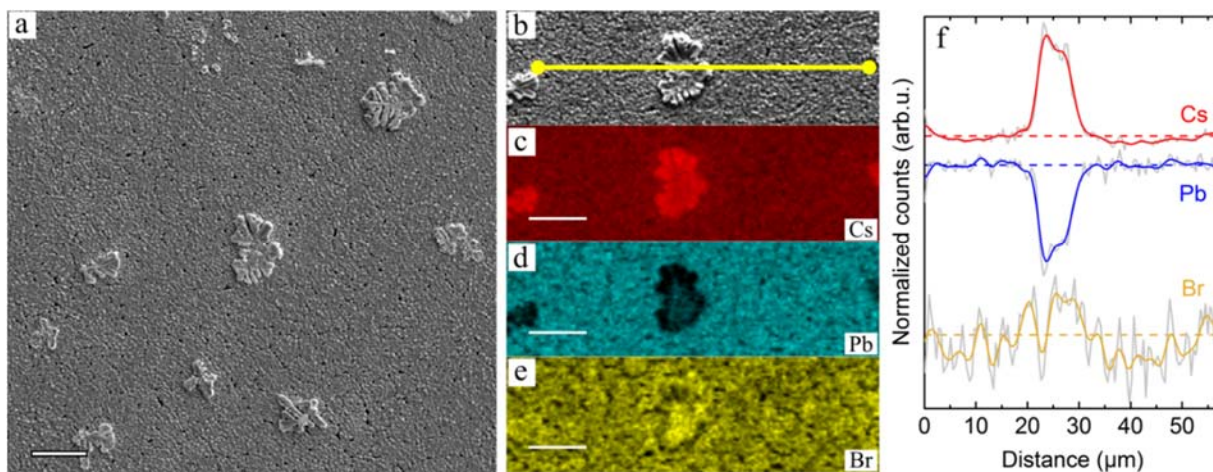
Figure 6. (a) SEM image of the Cs-Pb-Br film deposited with the two-step solution process. (b) Section of the SEM image showing the position of the profile in (f), along with the corresponding compositional maps showing the distribution of (c) Cs, (d) Pb and (e) Br. Note the secondary phase islands deposited on top of the film, which exhibit strong enhancement of Cs and depletion of Pb. All scale bars are 10 μm.

The CL maps measured on the same area (**Figure 7**) show that the film is homogeneously luminescent, with an optical transition at 2.35 eV, consistent with the $CsPbBr_3$ phase obtained from XRD. From the EDX counts and the phase identified by means of CL, we can match the stoichiometry of the islands to the Cs_4PbBr_6 phase. However, this assignment does not agree with the XRD pattern, in which no Cs_4PbBr_6 reflections were found. However, reflections for CsBr were measured, leading to the conclusion that the stoichiometry measured on the islands corresponds to $CsPbBr_3+3CsBr$. This is further confirmed by the CL and EDX maps acquired on a cross-section specimen (**Figure 8e-f and b-d, respectively**), showing homogeneous luminescence and elemental distribution across the film.
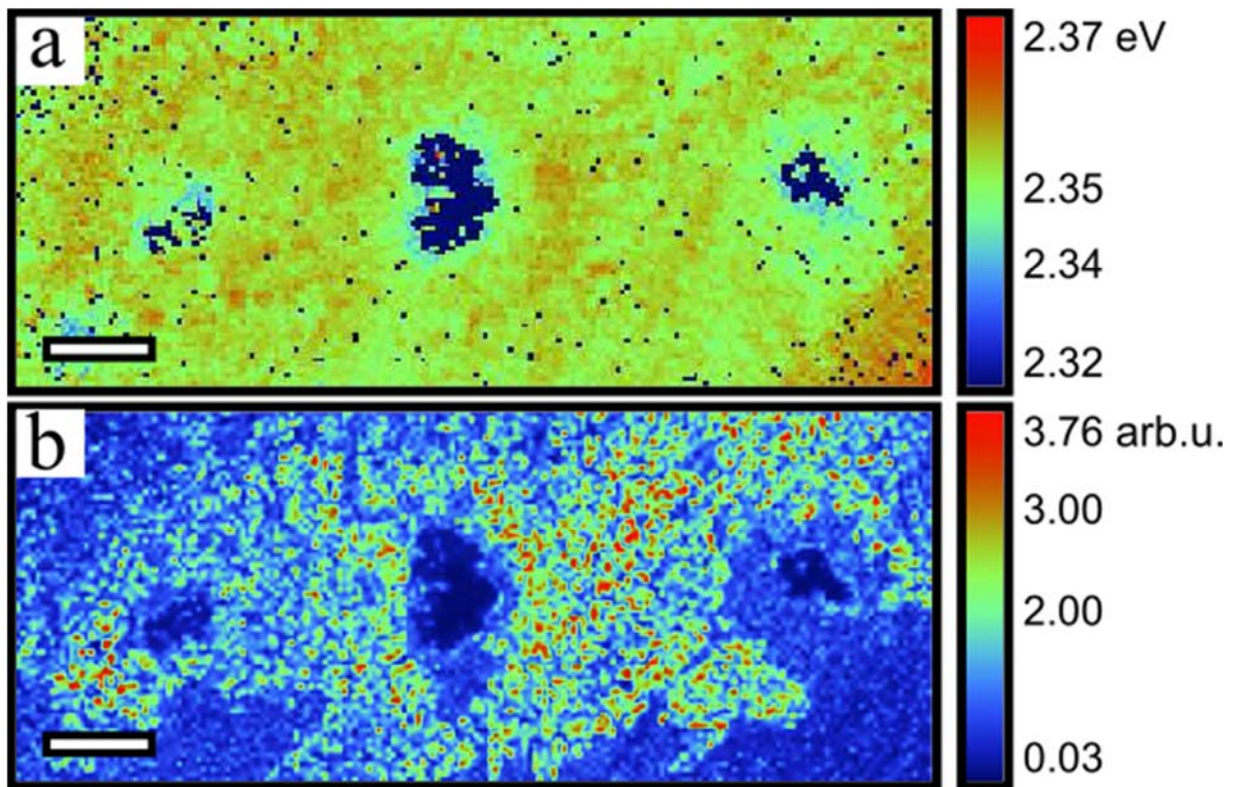

Figure 7. Maps of the optical properties of the Cs-Pb-Br film deposited with the two-step solution process shown in Figure 6a: (a) CL peak (energy of the optical transition) and (b) CL intensity. The islands on top of the film are dark in the visible range. All scale bars are 10 μm and the exposure time for the CL measurements was 10 ms.

The XRD pattern also contains reflections that match the $CsPb_2Br_5$ phase. We did not detect this

phase in our microscopic analysis. It is possible that the $PbBr_2$ film spin-coated in the first step is non-uniform and the reaction dynamics in the dipping step were inhomogeneous on the film, especially at the edges of the substrate. Because our microscopic sampling was localized mostly to the center of the substrate, we did not observe the $CsPb_2Br_5$ phase.
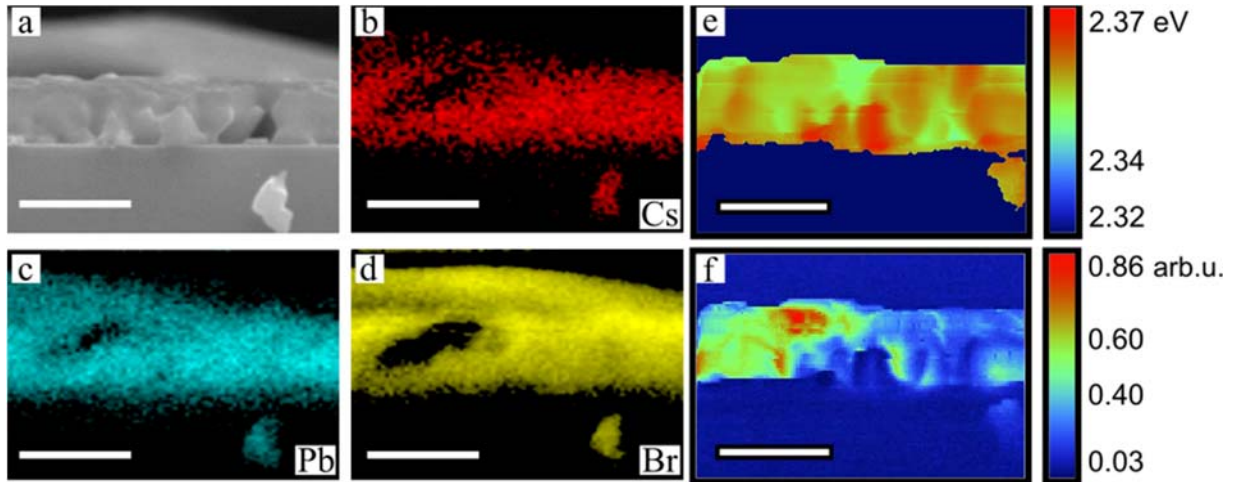
Figure 8. (a) SEM image of the cross-section of the Cs-Pb-Br film deposited with the two-step solution process and the corresponding compositional maps showing the distribution of (b) Cs, (c) Pb and (d) Br. No compositional changes are detected along the cross-section of the film. The CL maps of (e) CL emission peak position and (f) emission intensity, which show a rather uniform transition energy and intensity, corroborate the phase purity of the film. All scale bars are 1 μm and the exposure time for the CL measurements was 20 ms.

4.5   Coevaporated films

The surfaces of the films coevaporated on both glass and on Si substrates features micrometer-sized porous structures (**Figure 9a**; see details of these structures in Figure S2a and b). The structures are about 200-230 nm thicker than their surrounding closed film (see AFM topography in Figure 9b and c), which is about 720 nm thick (Figure S2c and d) with a roughness – measured in RMS of the height – of about 32 nm. These structures have the largest contribution to the film roughness: on average, the structures are 31 nm rough, while the roughness of the closed film regions is only 14 nm.
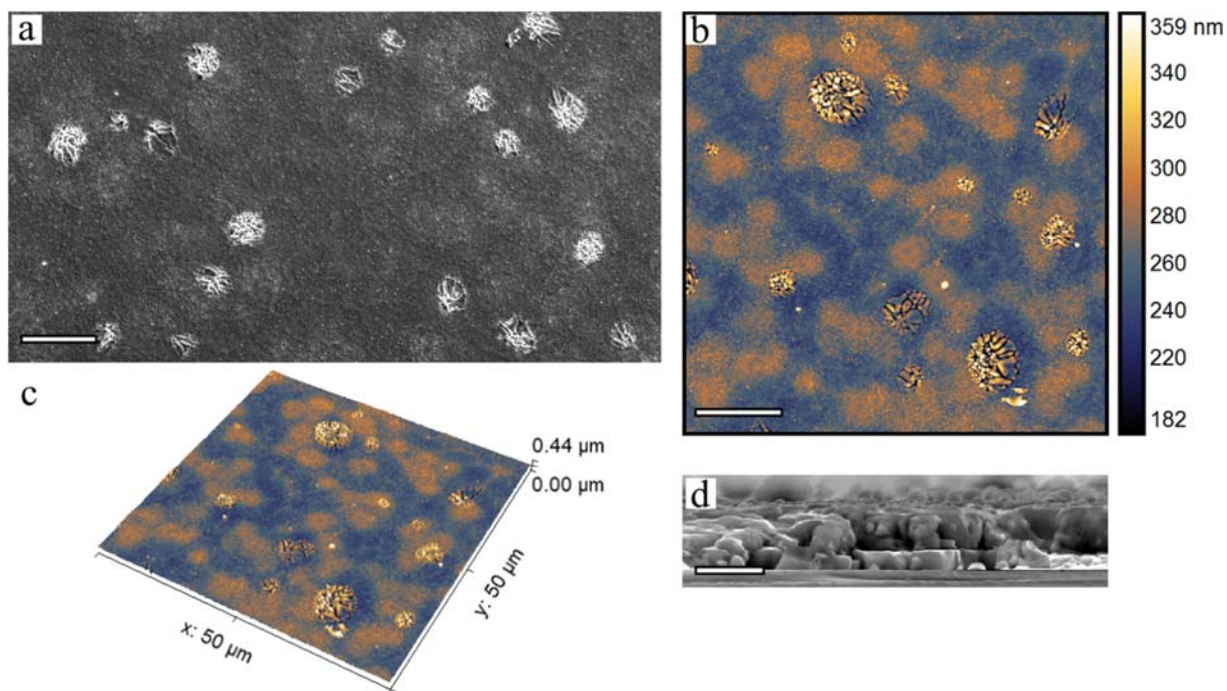
Figure 9. Morphology of a Cs-Pb-Br film coevaporated on a glass substrate: SEM images of the (a) surface and (d) cross-section, and AFM (b) image and (c) 3D topography. The coevaporation of CsBr and PbBr$_2$ forms a closed film with embedded micrometer-size structures. All scale bars are 10 μm.

We imaged the surface of the film and identified high-contrast regions localized to the cracks formed by the structures. On the flat film regions, the areas with smaller grains show higher contrast as well (see Figure S3 for the glass substrate and Figure S4 for the Si substrate). With CL we measured high-intensity radiative transitions that correlate well with these high contrast areas (**Figure 10**a and b). Two CL emission peaks were identified over the films: a low-intensity, broad band (characteristic of defect transitions[60]) around 1.8 eV (red band), which is dominant on large-grain areas (Figure 10b a and e); and a narrow, green emission peak, localized to the small-grain areas and the cracks in the structures (see magnified map in Figure 10f to h).

The accumulated CL spectrum over an area representative of the film's surface (Figure 10i) reveals some differences between the films coevaporated on glass and on Si substrates. The green emission of the film on glass is centered at 2.38 eV, while that of the sample on Si is centered at 2.35 eV. The latter transition is – as for the solution-based samples – consistent with the CsPbBr$_3$ phase and

18

the shifted peak at 2.38 eV is discussed below. However, the missing XRD reflections (see Section 4.1) do not support an unequivocal assignment of the CsPbBr$_3$ phase from a structural perspective. Therefore, we investigated the thin film deposited on Si by atom probe tomography (APT) to obtain quantitative information of the composition in atomic percentage.
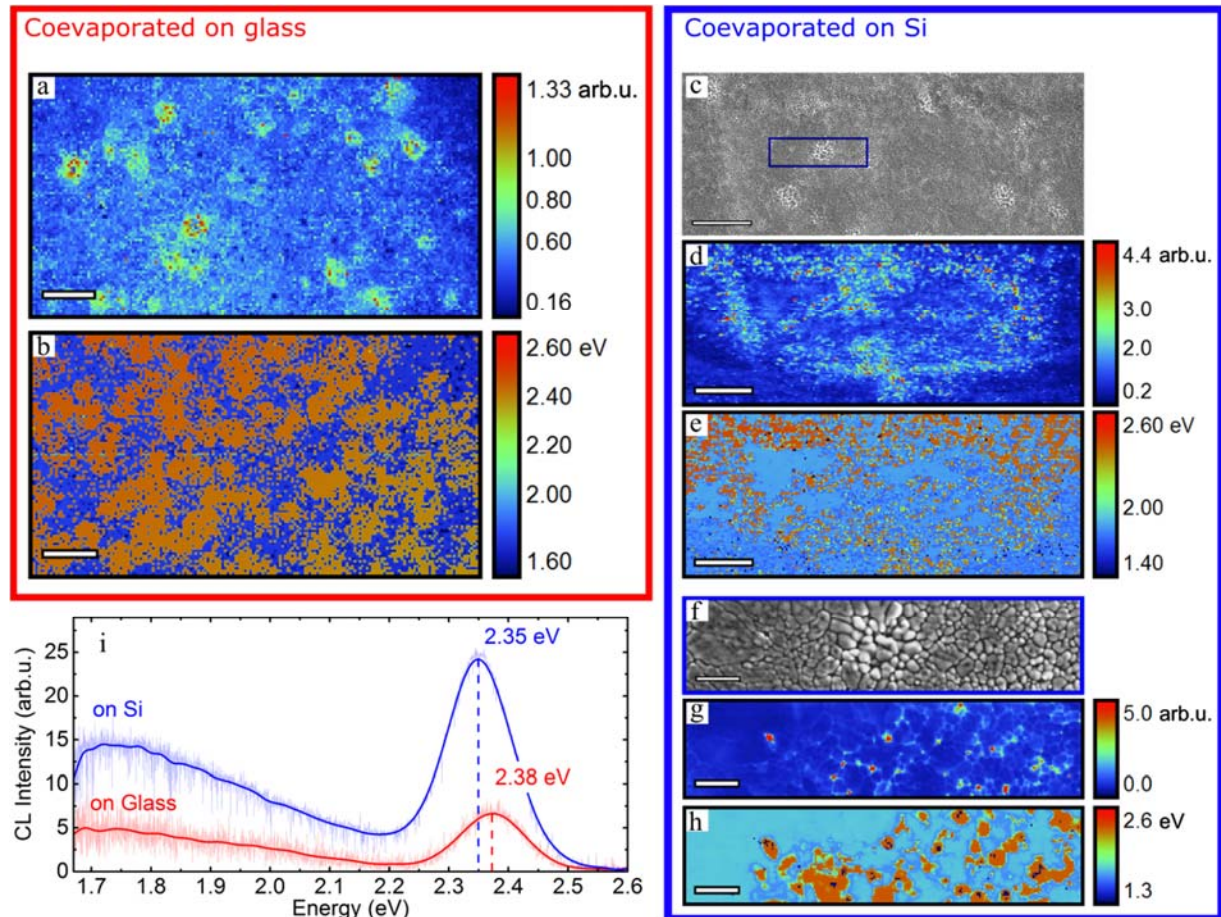
Figure 10. Optical properties of the Cs-Pb-Br films coevaporated on (a-b) glass and (c-h) Si substrates: (a) CL intensity map showing the distribution of the integrated visible luminescence intensity on the surface (area shown in Figure 9a) of the film coevaporated on glass. The intensity accounts for both the green (around 2.35 eV) and red (around 1.8 eV) bands, which are dominant in different areas of the film, as shown in (b). (c) SEM image of the surface of the film coevaporated on Si, and corresponding (e) CL intensity and (d) dominant emission peak distributions over the surface. (f) SEM image of a magnified region (shown in the blue rectangle), along with the corresponding (g) CL intensity and (h) emission peak distribution. Note that the green emission dominates in the small-grain areas and between the cracks of the structures. (i) Accumulated CL spectra of both films (on glass and Si), showing the slight blue shift and broadening of the green band for the film on glass. Scale bars in (a-e) are 10 μm and 2 μm in (f-h). The exposure time for the CL measurements was 100 ms for both films.

The APT investigation from **Figure 11** reveals three distinctive regions: i) a Br-rich surface with the average elemental concentrations of 15±2 at.% for Cs, 20±2 at.% for Pb, and 65±3 at.% for Br, ii) the expected $CsPbBr_3$ phase where the measured elemental concentrations are 20±2 at.% for Cs, 22±2 at.% for Pb, and 58±2 at.% for Br, and iii) a Cs-rich region with the average elemental concentrations of 28±2 at.% for Cs, 34±2 at.% for Pb, and 38±2 at.% for Br. The latter one does not correspond to any existing phases on the Cs-Pb-Br ternary diagram, which suggests that it might be a metastable phase. The APT results and the 2.35 eV luminescence from CL lead us to conclude that the luminescent phase is indeed the perovskite $CsPbBr_3$.

The variation of the optical transition from one substrate to the other is slightly above the thermal energy at room temperature. Since both samples were synthesized on the same run and measured using the same SEM parameters, this blue shift may not be negligible. One could expect to see compositional changes in the EDX maps, correlated to the different optoelectronic response on the surface, just as for the spin-coated sample. However, the elemental distribution is flat and uniform over the measured area for each element (see Figure S5).
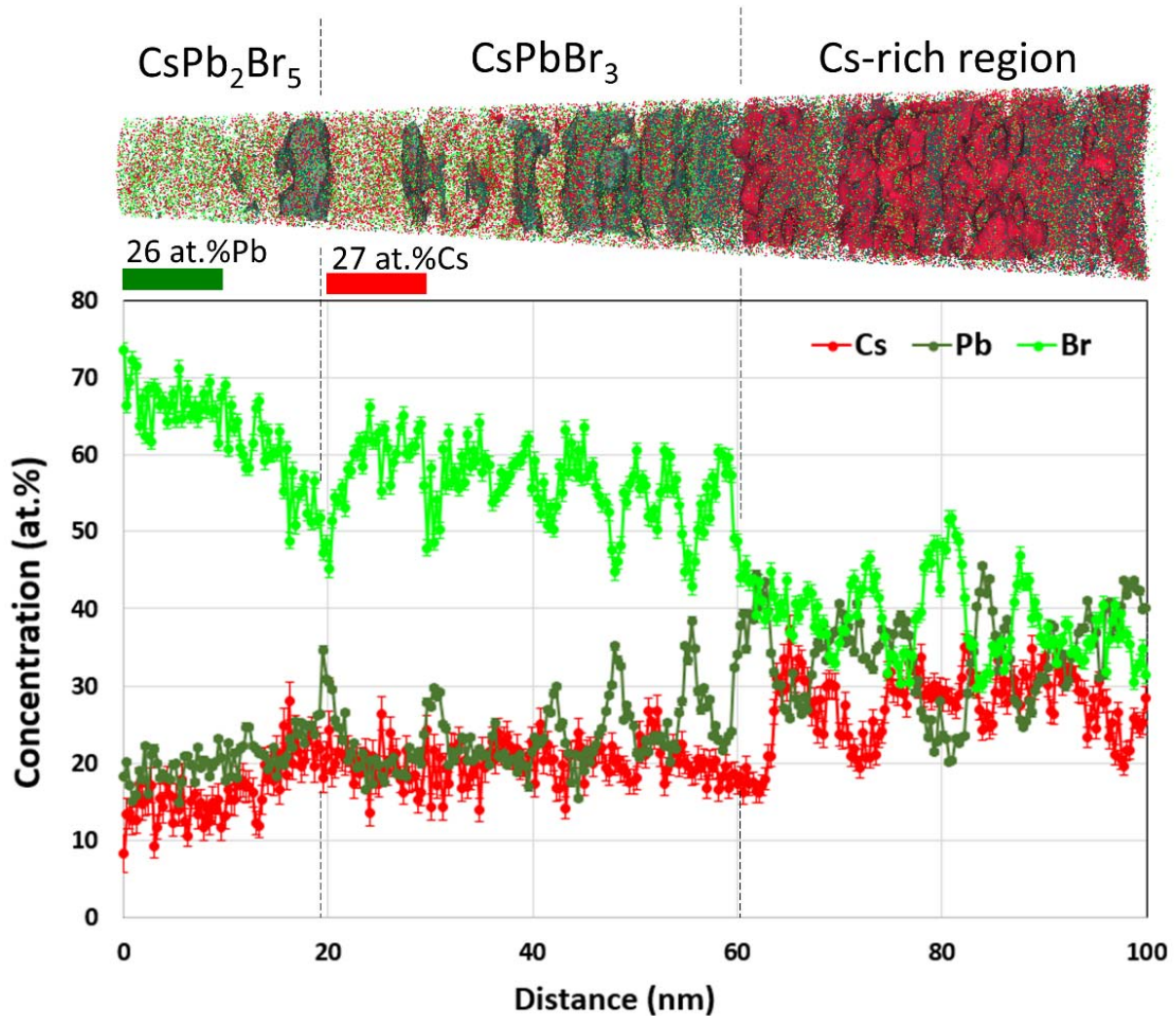
Figure 11. APT 3D elemental map together with the 1D concentration profiles for Br (light green), Pb (dark green), and Cs (reed) of the sample containing a coevaporated perovskite thin-film on a Si substrate. Beside the expected CsPbBr3 phase, this APT measurement reveals the presence of a Br-rich surface which approaches the composition of CsPb2Br5 phase and of a Cs-rich region deep inside the sample. The latter one could not be correlated to any existing phases on the Cs-Pb-Br ternary diagram.

Because the surface EDX and CL maps do not reconcile, and because the green luminescence is localized to the cracks, especially for the film on Si (Figure 10g and h), we measured the cleaved cross-section of both films. On the CL maps (**Figure 12b, c, e-g**), we identified two layers with different optical transitions for both substrates: a layer directly above the substrate exhibiting green emission at 2.35 eV, which corresponds to the CsPbBr3 phase, and a surface layer with a dominant

21

broad red emission band at 1.8 eV with a quenched green emission peak. The green-emitting layer in the film on glass is thinner than that of the film on Si. This explains the 2.38 eV green emission in the accumulated spectrum from the surface of the film on glass.
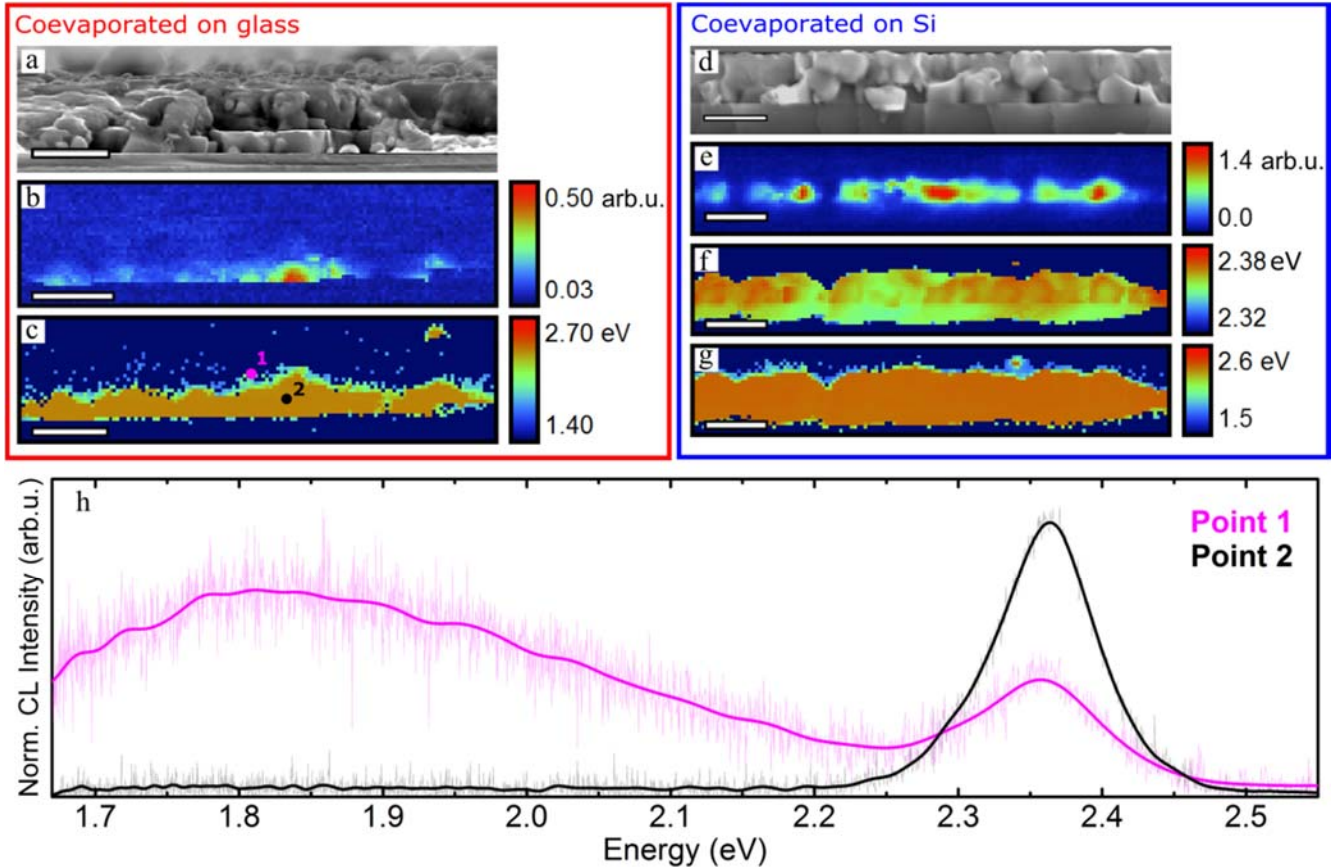

Figure 12. Optical properties along a cross-section of the Cs-Pb-Br films coevaporated on glass (a-c) and Si (d-g): (a) SEM image, (b) corresponding CL intensity, and (c) dominant emission peak maps of the film coevaporated on glass. The film exhibits a bottom layer, which is highly luminescent in the green region of the spectrum. Low-intensity red luminescence characterize the surface layer, as shown in the (h) normalized CL spectra of points 1 and 2 in (c). (d) SEM image of the cross-section of the film coevaporated on Si. The corresponding (e) CL intensity and (f and g) emission peak distribution show a similar layering as in the film coevaporated on glass. (f) and (g) are representations of the same data with a different energy span. The map in (f) shows the thickness and variation of the green-luminescent bottom layer, whereas the map in (g) also shows the red-luminescent surface layer.

Because the electron beam can only excite a limited surface volume of the film at a given acceleration voltage, the CL signal of the surface measurement is generated at the interface between the $CsPbBr_3$ bottom layer and a highly defective surface layer. We rationalize the slight blue shift

as the effect of tensile strain at that interface. This effect is similar to the blue shift in the excitonic emission peaks reported in ref. [61] and is explained by the anti-bonding nature of the valence band maximum of $CsPbX_3$ compounds.[58,62] The broadening that the green emission peak suffers on the surface spectra of the film on glass is probably because of ensemble averaging of the different depths excited with the electron beam. All these effects are reduced in the film on Si due to the thicker $CsPbBr_3$ bottom layer.

Having established the bottom layer as $CsPbBr_3$, we used EDX maps and linescans to determine the relative composition and phase distribution of the surface layer. The EDX maps in **Figure 13b-d** show that the surface layer of the film coevaporated on glass exhibits a rather homogeneous elemental distribution with a slight Pb enrichment and a more pronounced Cs depletion, as compared with the $CsPbBr_3$ bottom layer. The elemental distribution of the film on Si is similar, but with an even more pronounced Pb enrichment towards the surface. These EDX results can be further supported by the APT results, where the uppermost layer of the perovskite film was found to be depleted in Cs, but strongly enriched in Br (see Figure 11). We note here that the deviation in Pb behavior between EDX and APT might be due to the fact that EDX probes large volumes when comparing with APT where very small volumes (in nm^3) are probed.
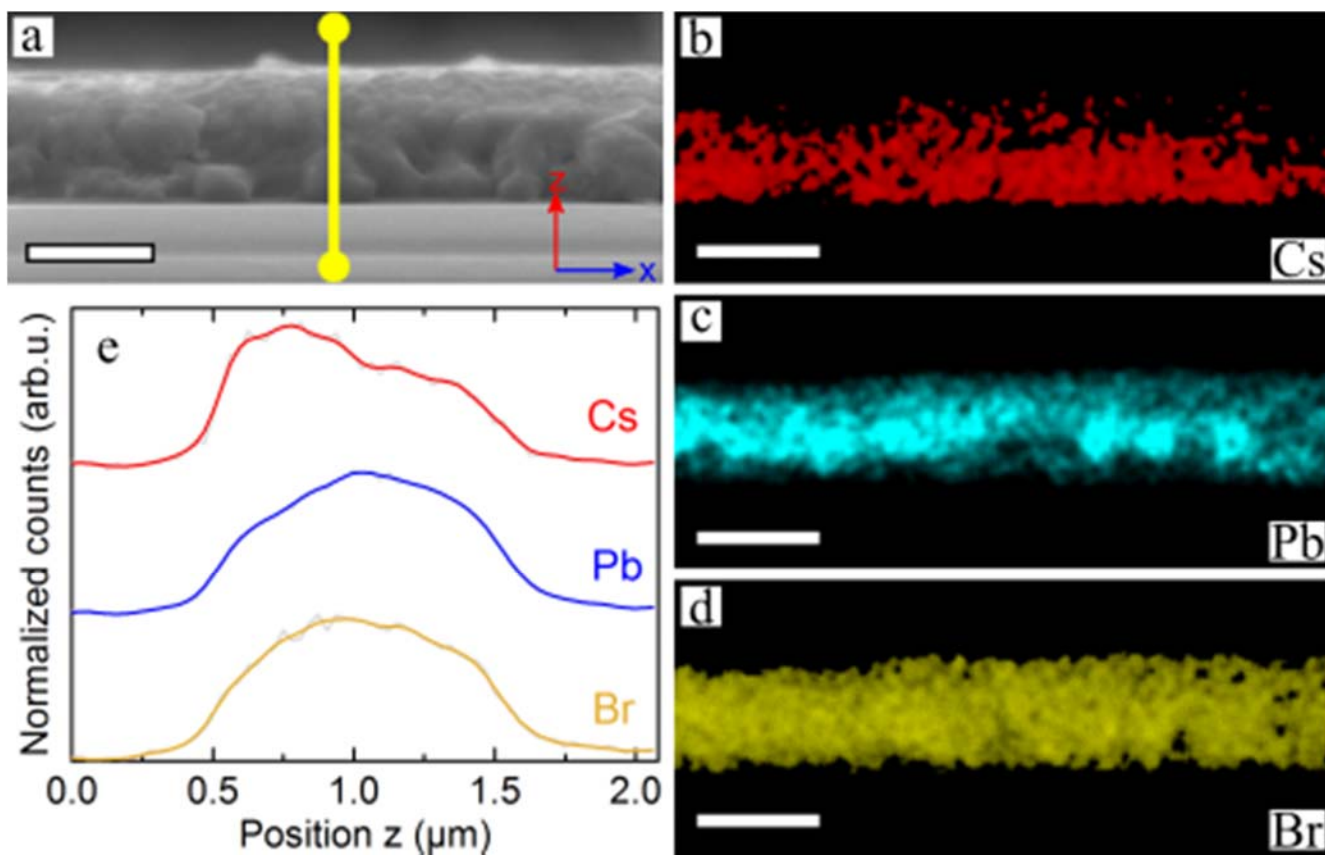
Figure 13. Composition of the Cs-Pb-Br film coevaporated on glass: (a) SEM image of the cross-section showing the path used to obtain the EDX linescan in (e), and the corresponding compositional maps, showing the distribution of (b) Cs, (c) Pb and (d) Br. The surface layer exhibits a Cs enhancement, associated with Cs decrease in the $CsPb_2Br_5$ secondary phase. All scale bars are 1 μm.

This substrate-related effect has not been studied in depth in the present paper, but we believe that the thermal conductivity of the substrate influences the dynamics of conversion in the post-deposition annealing step. The relative stoichiometry of the surface layer matches with that of the Pb-rich ternary phase $CsPb_2Br_5$. This phase assignment agrees with our XRD results and the 1.8 eV defect transition measured with CL, as $CsPb_2Br_5$ has a wide bandgap and the observed emission has been reported to stem from recombination at deep traps.[63] We assign the Pb accumulation on the surface of the film on Si to a thin layer of excess $PbBr_2$ after the post-deposition annealing.

4.6 Coevaporated films on a carbon-coated Cu grid

Figure 14a shows the superposition of 225 ED patterns from a 10 μm^2 area of the 70 nm thin film.

In Figure 14b, we compare the azimuthal integration of the ED of the thin film to the XRD pattern

of the reference powder. The film's structure agrees with the $CsPbBr_3$ reference. Additional peaks

can be assigned to minor $CsPbBr_3$ reflections, invisible in the XRD pattern of the reference, and to

a small contribution of $CsPb_2Br_5$.
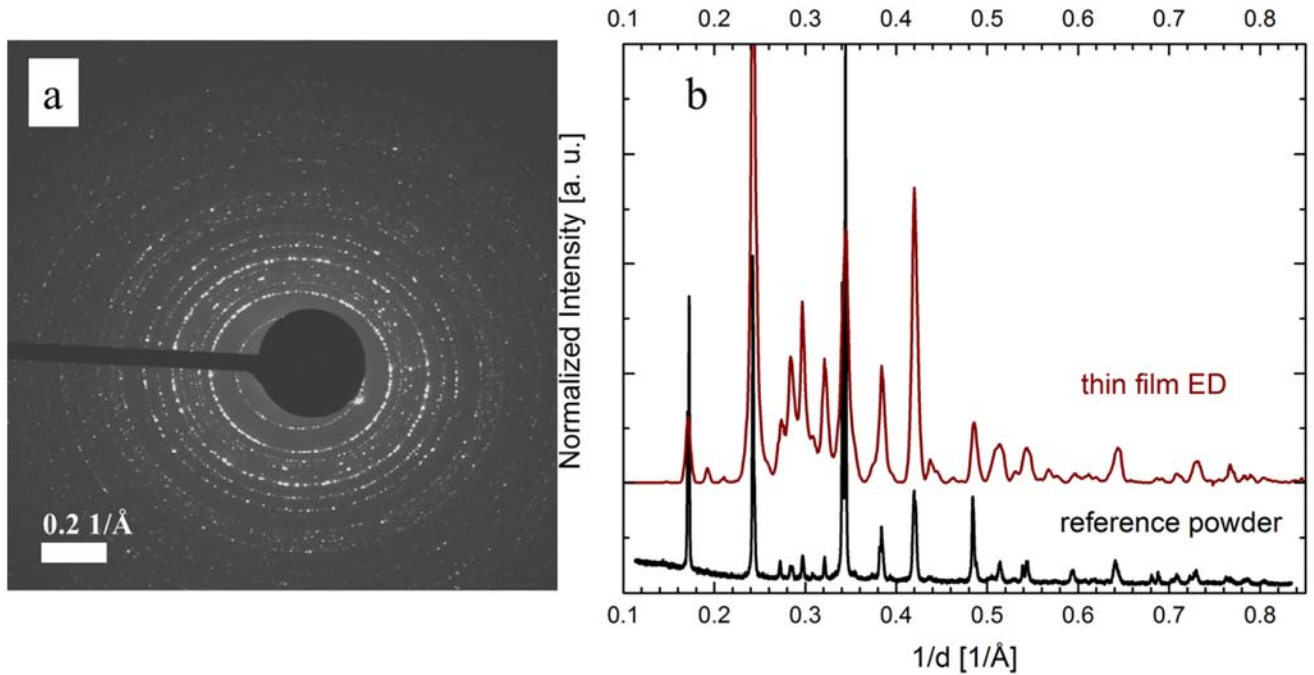
Figure 14. (a) Superposition of selected area ED patterns, covering an area of 10 μm^2 of the coevaporated 70nm thin film (elliptical due to a microscope artifact). (b) Integrated intensity of ED patterns of the thin film and XRD pattern of the reference $CsPbBr_3$ powder as a function of the reciprocal lattice. The elliptical artifact was corrected using the ProcessDiffraction Software.[24]

The average grain size is between 50 and 100 nm, as shown in the TEM images (**Figure 15**a).

Islands above 1000 nm in size are also visible. Even though the statistics for a film that is 70 nm

thick are poor, EDX measurements show that the islands are Pb-rich, as compared with the

surrounding grains. In addition, they do not exhibit any luminescence emission measurable in the

probed spectral range. In contrast, the surrounding grains have a sharp optical transition at 2.35 eV

(Figure 15d), consistent with the optical transitions found for the solution-processed and the thick

coevaporated films. These results confirm that the grains are $CsPbBr_3$, while the precipitates are

identified as single grains of $CsPb_2Br_5$ by scanning transmission electron microscopy (STEM)-ED
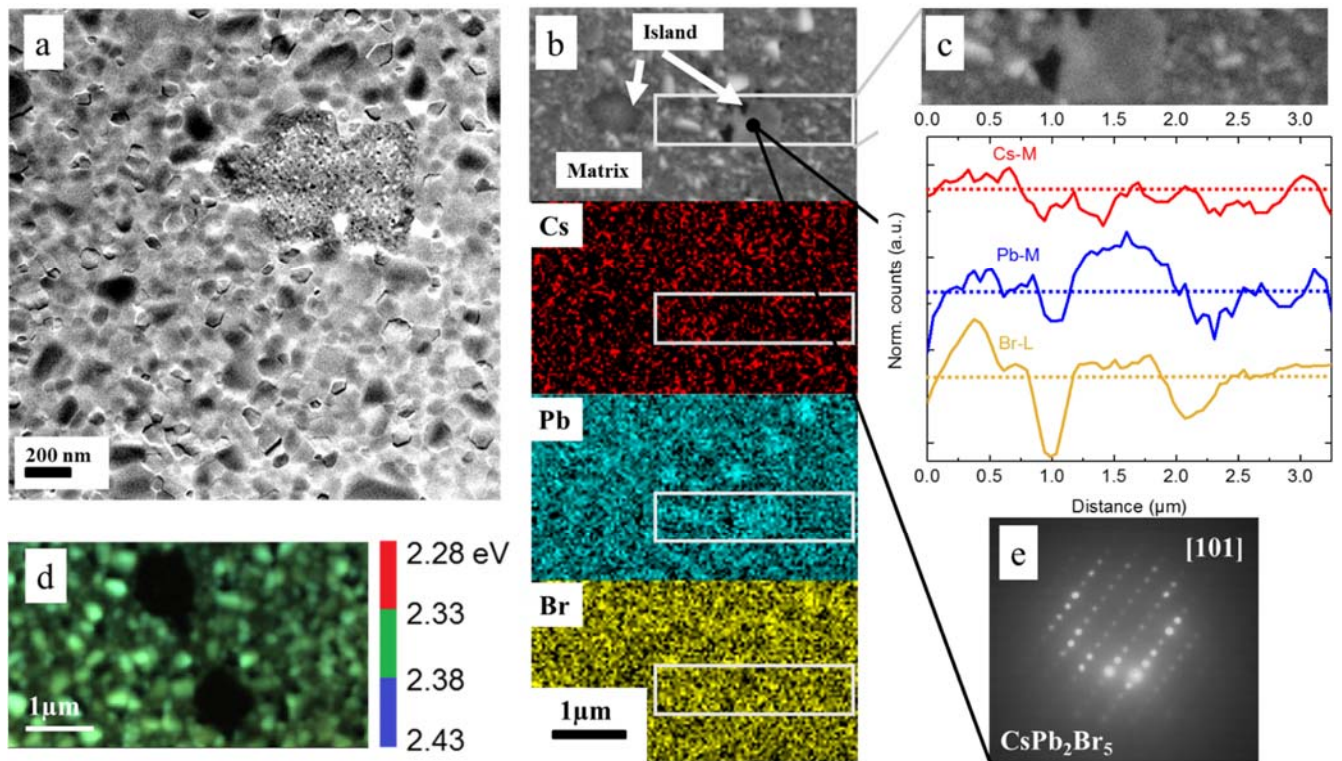
(Figure 15e).

Figure 15: Correlative analysis of the co-evaporated 70 nm thin film on a carbon-coated Cu-TEM-Grid. (a) TEM bright field image showing a closed film with an island; (b) SEM image with EDX maps; (c) EDX linescan and (d) CL map; (e) STEM-ED pattern of an island acquired in a SEM at 30 kV.

5. Discussion

As described in detail in the previous Section 4, all analyzed films contain secondary phases, not only at scales on the order of 100 nm to 1 μm, but also at smaller scales (10 nm). We provide a summary of all findings in **Figure 16**. As shown, the composition of phases (binary or ternary), as well as their spatial distributions, seem to depend on the deposition type (solution-based, coevaporated), but also on the substrate material and on the deposition recipe. The presence of various Cs-Pb-Br phases in an intendedly single-phase thin film can be explained by the similar formation enthalpies for all Cs-Pb-Br ternary phases (Section 4.2). Again, we note that we cannot generalize our results in terms of same materials properties for all Cs-Pb-Br thin films synthesized

under the same growth conditions. Nevertheless, it was found reproducibly that the spatial distributions of secondary phases in solution-based thin films do not exhibit a preferential direction; the secondary phases tend to form precipitates within the thin film or on the surface. In contrast, secondary phases in the coevaporated Cs-Pb-Br studied in the present work are distributed in a layered manner, with a homogeneous $CsPbBr_3$ bottom layer and $CsPb_2Br_5$ on top.
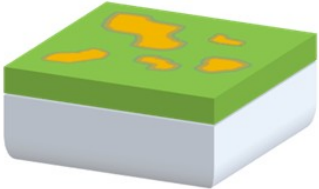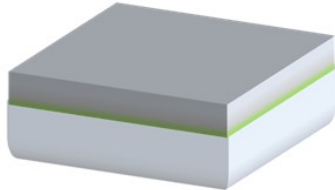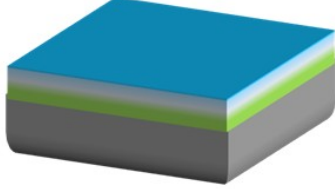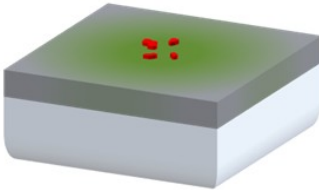

Figure 16: Summary of the samples analyzed in the present work, the phases found, and their distribution as identified by means of our correlative microscopy approach. The sizes of the secondary phase domains are not to scale. See text for a detailed discussion

The reproducibly detected layered arrangement of phases in the coevaporated films suggests reaction kinetics specific for the coevaporation deposition process. It is noteworthy that recent reports highlighted $CsPb_2Br_5$ as a passivation material for $CsPbBr_3$-based devices, with improvements of device performance and long-term stability under ambient conditions.[43,64,65] These results are in good agreement with the enhancement of the PL intensity in the $CsPb_2Br_5$-

containing, coevaporated $CsPbBr_3$ films (see Figure S6). However, the exact mechanism by which $CsPb_2Br_5$ passivation improves the performance and stability of the devices remains unknown.

6. Conclusions

We investigated structural, compositional, and optoelectronic properties of various inorganic Cs-Pb-Br thin films by means of XRD, PL spectroscopy, and a variety of spatially resolved SEM and TEM methods. The correlative analysis of the characterized thin films shows that none of these layers exhibited only one single Cs-Pb-Br phase. Indeed, DFT calculations confirm that the three ternary phases ($CsPbBr_3$, $CsPb_2Br_5$, Cs_4PbBr_6) all have similar formation enthalpies, which explains why slight variations of the deposition conditions may lead to a substantial change in the Cs-Pb-Br phase composition (involving the ternary and also the binary CsBr and $PbBr_2$ phases), with spatial distributions and volume fractions varying considerably for different synthesis methods. By means of correlative SEM and TEM, we found that secondary phases are even present at the nanoscale, beyond the detection limit of XRD. This calls for further research on the nanoscale phase distribution of (seemingly) single-phase Cs-Pb-Br films, and on its reproducibility in films grown by different deposition recipes.

Supporting Information

The following files are available free of charge.

EDX counts table, additional in-lens SEM, AFM images, absorption and PL spectra (PDF)

AUTHOR INFORMATION

Corresponding Author

* hannah.funk@helmholtz-berlin.de, Tel: +49 30 2093 7658

Present Addresses

†If an author's address is different than the one given in the affiliation line, this information may be included here.

Author Contributions

The manuscript was written through contributions of all authors. All authors have given approval to the final version of the manuscript.

‡These authors contributed equally.

References

(1)   Green, M. A.; Hishikawa, Y.; Dunlop, E. D.; Levi, D. H.; Hohl-Ebinger, J.; Ho-Baillie, A. W. Y. Solar Cell Efficiency Tables (Version 52). *Prog. Photovoltaics Res. Appl.* **2018**, *26*, 427–436.

(2)   Correa-Baena, J. P.; Abate, A.; Saliba, M.; Tress, W.; Jesper Jacobsson, T.; Grätzel, M.; Hagfeldt, A. The Rapid Evolution of Highly Efficient Perovskite Solar Cells. *Energy Environ. Sci.* **2017**, *10*, 710–727.

(3)   Brenner, T. M.; Egger, D. A.; Kronik, L.; Hodes, G.; Cahen, D. Hybrid Organic— Inorganic Perovskites: Low-Cost Semiconductors with Intriguing Charge-Transport Properties. *Nat. Rev. Mater.* **2016**, *1*, 15007.

(4)   Saliba, M.; Correa-Baena, J. P.; Grätzel, M.; Hagfeldt, A.; Abate, A. Perovskite Solar Cells: From the Atomic Level to Film Quality and Device Performance. *Angew. Chemie - Int. Ed.* **2018**, *57*, 2554–2569.

(5)   Kulbak, M.; Cahen, D.; Hodes, G. How Important Is the Organic Part of Lead Halide Perovskite Photovoltaic Cells? Efficient $CsPbBr_3$Cells. *J. Phys. Chem. Lett.* **2015**, *6*, 2452–2456.

(6)   Kulbak, M.; Gupta, S.; Kedem, N.; Levine, I.; Bendikov, T.; Hodes, G.; Cahen, D. Cesium Enhances Long-Term Stability of Lead Bromide Perovskite-Based Solar Cells. *J. Phys. Chem. Lett.* **2016**, *7*, 167–172.

(7)   Yantara, N.; Bhaumik, S.; Yan, F.; Sabba, D.; Dewi, H. A.; Mathews, N.; Boix, P. P.; Demir, H. V.; Mhaisalkar, S. Inorganic Halide Perovskites for Efficient Light-Emitting Diodes. *J. Phys. Chem. Lett.* **2015**, *6*, 4360–4364.

(8)   Ng, Y. F.; Jamaludin, N. F.; Yantara, N.; Li, M.; Irukuvarjula, V. K. R.; Demir, H. V.; Sum, T. C.; Mhaisalkar, S.; Mathews, N. Rapid Crystallization of All-Inorganic CsPbBr$_3$ Perovskite for High-Brightness Light-Emitting Diodes. *ACS Omega* **2017**, *2*, 2757–2764.

(9)   Li, J.; Xu, L.; Wang, T.; Song, J.; Chen, J.; Xue, J.; Dong, Y.; Cai, B.; Shan, Q.; Han, B.; et al. 50-Fold EQE Improvement up to 6.27% of Solution-Processed All-Inorganic Perovskite CsPbBr$_3$ QLEDs via Surface Ligand Density Control. *Adv. Mater.* **2017**, *29* (5), 1603885.

(10)   Stoumpos, C. C.; Malliakas, C. D.; Peters, J. A.; Liu, Z.; Sebastian, M.; Im, J.; Chasapis, T. C.; Wibowo, A. C.; Chung, D. Y.; Freeman, A. J.; et al. Crystal Growth of the Perovskite Semiconductor CsPbBr 3 : A New Material for High-Energy Radiation Detection. Cryst. Growth Des. 2013, 13, 2722−2727.

(11)   Rakita, Y.; Kedem, N.; Gupta, S.; Sadhanala, A.; Kalchenko, V.; Böhm, M. L.; Kulbak, M.; Friend, R. H.; Cahen, D.; Hodes, G. Low-Temperature Solution-Grown CsPbBr$_3$ Single Crystals and Their Characterization. *Cryst. Growth Des.* **2016**, *16*, 5717–5725.

(12)   Chen, M.; Zou, Y.; Wu, L.; Pan, Q.; Yang, D.; Hu, H.; Tan, Y.; Zhong, Q.; Xu, Y.; Liu, H.; et al. Solvothermal Synthesis of High-Quality All-Inorganic Cesium Lead Halide Perovskite Nanocrystals: From Nanocube to Ultrathin Nanowire. *Adv. Funct. Mater.* **2017**, *27*, 1701121.

(13)   Moller, C. K. Crystal Structure and Photoconductivity of Caesium Plumbohalides. *Nature* **1958**, *182*, 1436.

(14)   Moller, C. K. The Structure Of Perovskite-Like Cæsium Plumbo Trihalides. *Mat. Fys. Medd. Dan. Vid. Selsk* **1959**, *32*, 1.

(15)   Rodová, M.; Brožek, J.; Nitsch, K. Phase Transitions in Ternary Caesium Lead Bromide. *J. Therm. Anal.* **2003**, *71*, 667–673.

(16)   Khenkin, M. V.; K. M., A.; Visoly-Fisher, I.; Kolusheva, S.; Galagan, Y.; Di Giacomo, F.; Vukovic, O.; Patil, B. R.; Sherafatipour, G.; Turkovic, V.; et al. Dynamics of Photoinduced Degradation of Perovskite Photovoltaics: From Reversible to Irreversible Processes. *ACS Appl. Energy Mater.* **2018**, *1* (2), 799–806.

(17)   Cola, M.; Riccardi, R. Binary Systems Formed by Lead Bromide with (Li, Na, K, Rb, Cs and Tl) Br: A DTA and Diffractometric Study. *Zeitschrift für Naturforsch. A* **1971**, *26*, 1328.

(18)   Kuznetsova, I. Y.; Kovaleva, I. S.; Fedorov, V. A. Interaction of Lead Bromide with Cesium and Cadmium Bromides. *Zhurnal Neorg. Khimii* **2001**, *46*, 1900–1905.

(19)   Zaitseva, I. Y.; Kovaleva, I. S.; Fedorov, V. A. $HgBr_2$-$CsPbBr_3$ and $CsHgBr_3$-$PbBr_2$ Joins of the $HgBr_2$-$PbBr_2$-CsBr System. *Russ. J. Inorg. Chem.* **2006**, *51*, 619–623.

(20)   Hirotsu, S.; Harada, J.; Iizumi, M.; Gesi, K. Structural Phase Transitions in $CsPbBr_3$. *J. Phys. Soc. Japan* **1974**, *37*, 1393–1398.

(21)   Hirotsu, S.; Suzuki, T.; Sawada, S. Ultrasonic Velocity around the Successive Phase Transition Points of $CsPbBr_3$. *J. Phys. Soc. Japan* **1977**, *43*, 575–582.

(22)   Udayabhaskararao, T.; Houben, L.; Cohen, H.; Menahem, M.; Pinkas, I.; Avram, L.; Wolf, T.; Teitelboim, A.; Leskes, M.; Yaffe, O.; et al. A Mechanistic Study of Phase Transformation in Perovskite Nanocrystals Driven by Ligand Passivation. *Chem. Mater.* **2018**, *30*, 84–93.

(23)   Velázquez, M.; Ferrier, A.; Péchev, S.; Gravereau, P.; Chaminade, J. P.; Portier, X.;

Moncorgé, R. Growth and Characterization of Pure and Pr^{3+}-Doped Cs_4PbBr_6 Crystals. *J. Cryst. Growth* **2008**, *310*, 5458–5463.

(24)   Lábár, J. L. Electron Diffraction Based Analysis of Phase Fractions and Texture in Nanocrystalline Thin Films, Part I: Principles. *Microsc. Microanal.* **2008**, *14*, 287–295.

(25)   Nečas, D.; Klapetek, P. Gwyddion: An Open-Source Software for SPM Data Analysis. *Cent. Eur. J. Phys.* **2012**, *10*, 181–188.

(26)   Kelly, T. F.; Larson, D. J.; Thompson, K.; Alvis, R. L.; Bunton, J. H.; Olson, J. D.; Gorman, B. P. Atom Probe Tomography of Electronic Materials. *Annu. Rev. Mater. Res.* **2007**, *37*, 681–727.

(27)   Perdew, J. P.; Burke, K.; Ernzerhof, M. Generalized Gradient Approximation Made Simple. *Phys. Rev. Lett.* **1996**, *77*, 3865–3868.

(28)   Tkatchenko, A.; Scheffler, M. Accurate Molecular van Der Waals Interactions from Ground-State Electron Density and Free-Atom Reference Data. *Phys. Rev. Lett.* **2009**, *102*, 6–9.

(29)   Bučko, T.; Lebègue, S.; Hafner, J.; Ángyán, J. G. Improved Density Dependent Correction for the Description of London Dispersion Forces. *J. Chem. Theory Comput.* **2013**, *9*, 4293–4299.

(30)   Bučko, T.; Lebègue, S.; Ángyán, J. G.; Hafner, J. Extending the Applicability of the Tkatchenko-Scheffler Dispersion Correction via Iterative Hirshfeld Partitioning. *J. Chem. Phys.* **2014**, *141*, 034114.

(31)   Kresse, G.; Fortmüller, J. Efficient Iterative Schemes for Ab Initio Total-Energy Calculations Using a Plane-Wave Basis Set. *Phys. Rev. B - Condens. Matter Mater. Phys.*

1996, *54*,11169–11186.

(32)   Kresse, G.; Joubert, D. From Ultrasoft Pseudopotentials to the Projector Augmented-Wave

Method. *Phys. Rev. B - Condens. Matter Mater. Phys.* **1999**, *59*, 1758–1775.

(33)   Bučko, T.; Hafner, J.; Ángyán, J. G. Geometry Optimization of Periodic Systems Using

Internal Coordinates. *J. Chem. Phys.* **2005**, *122*, 124508.

(34)   Lumbreras, M.; Protas, J.; Jebbari, S.; Dirksen, G. J.; Schoonman, J. Structure and Ionic

Conductivity of Mixed Lead Halides $PbCl_{2x}Br_{2(1-x)}$. II. *Solid State Ionics* **1986**, *20*, 295–

304.

(35)   Wyckoff, R. W. G. CsCl Structure, Cesium Chloride Structure. In *Crystal Structures*;

Interscience Publishers: New York, 1963; pp 85–237.

(36)   Zhang, D.; Eaton, S. W.; Yu, Y.; Dou, L.; Yang, P. Solution-Phase Synthesis of Cesium

Lead Halide Perovskite Nanowires. *J. Am. Chem. Soc.* **2015**, *137*, 9230–9233.

(37)   Yin, J.; Yang, H.; Song, K.; El-Zohry, A. M.; Han, Y.; Bakr, O. M.; Brédas, J. L.;

Mohammed, O. F. Point Defects and Green Emission in Zero-Dimensional Perovskites. *J.

Phys. Chem. Lett.* **2018**, *9*, 5490–5495.

(38)   Fejfar, A.; Hývl, M.; Vetushka, A.; Pikna, P.; Hájková, Z.; Ledinský, M.; Kočka, J.;

Klapetek, P.; Marek, A.; Mašková, A.; et al. Correlative Microscopy of Radial Junction

Nanowire Solar Cells Using Nanoindent Position Markers. *Sol. Energy Mater. Sol. Cells*

2015, *135*, 106–112.

(39)   Abou-Ras, D. Correlative Microscopy Analyses of Thin-Film Solar Cells at Multiple

Scales. *Mater. Sci. Semicond. Process.* **2017**, *65*, 35–43.

(40)   Nitsch, K.; Hamplová, V.; Nikl, M.; Polák, K.; Rodová, M. Lead Bromide and Ternary

Alkali Lead Bromide Single Crystals - Growth and Emission Properties. *Chem. Phys. Lett.* **1996**, *258*, 518–522.

(41)   Akkerman, Q. A.; Motti, S. G.; Srimath Kandada, A. R.; Mosconi, E.; D'Innocenzo, V.; Bertoni, G.; Marras, S.; Kamino, B. A.; Miranda, L.; De Angelis, F.; et al. Solution Synthesis Approach to Colloidal Cesium Lead Halide Perovskite Nanoplatelets with Monolayer-Level Thickness Control. *J. Am. Chem. Soc.* **2016**, *138*, 1010–1016.

(42)   Liang, J.; Liu, J.; Jin, Z. All-Inorganic Halide Perovskites for Optoelectronics: Progress and Prospects. *Sol. RRL* **2017**, *1*, 1770138.

(43)   Lei, J.; Gao, F.; Wang, H.; Li, J.; Jiang, J.; Wu, X.; Gao, R.; Yang, Z.; Liu, S. (Frank). Efficient Planar $CsPbBr_3$ perovskite Solar Cells by Dual-Source Vacuum Evaporation. *Sol. Energy Mater. Sol. Cells* **2018**, *187*, 1–8.

(44)   Chen, D.; Wan, Z.; Chen, X.; Yuan, Y.; Zhong, J. Large-Scale Room-Temperature Synthesis and Optical Properties of Perovskite-Related Cs_4PbBr_6 Fluorophores. *J. Mater. Chem. C* **2016**, *4*, 10646–10653.

(45)   Zhang, H.; Liao, Q.; Wu, Y.; Chen, J.; Gao, Q.; Fu, H. Pure Zero-Dimensional Cs_4PbBr_6 Single Crystal Rhombohedral Microdisks with High Luminescence and Stability. *Phys. Chem. Chem. Phys.* **2017**, *19*, 29092–29098.

(46)   Zhang, Y.; Saidaminov, M. I.; Dursun, I.; Yang, H.; Murali, B.; Alarousu, E.; Yengel, E.; Alshankiti, B. A.; Bakr, O. M.; Mohammed, O. F. Zero-Dimensional Cs_4PbBr_6 Perovskite Nanocrystals. *J. Phys. Chem. Lett.* **2017**, *8*, 961–965.

(47)   Cha, J.-H. H.; Han, J. H.; Yin, W.; Park, C.; Park, Y.; Ahn, T. K.; Cho, J. H.; Jung, D.-Y. Y. Photoresponse of $CsPbBr_3$ and Cs_4PbBr_6 Perovskite Single Crystals. *J. Phys. Chem.*

Lett. **2017**, *8*, 565–570.

(48)   Seth, S.; Samanta, A. Fluorescent Phase-Pure Zero-Dimensional Perovskite-Related

Cs$_4$PbBr$_6$ Microdisks: Synthesis and Single-Particle Imaging Study. *J. Phys. Chem. Lett.*

2017, *8*, 4461–4467.

(49)   De Bastiani, M.; Dursun, I.; Zhang, Y.; Alshankiti, B. A.; Miao, X. H.; Yin, J.; Yengel, E.;

Alarousu, E.; Turedi, B.; Almutlaq, J. M.; et al. Inside Perovskites: Quantum

Luminescence from Bulk Cs$_4$PbBr$_6$ Single Crystals. *Chem. Mater.* **2017**, *29*, 7108–7113.

(50)   Yin, J.; Zhang, Y.; Bruno, A.; Soci, C.; Bakr, O. M.; Brédas, J. L.; Mohammed, O. F.

Intrinsic Lead Ion Emissions in Zero-Dimensional Cs$_4$PbBr$_6$ Nanocrystals. *ACS Energy*

Lett. **2017**, *2*, 2805–2811.

(51)   Nikl, M.; Mihokova, E.; Nitsch, K.; Somma, F.; Giampaolo, C.; Pazzi, G. .; Fabeni, P.;

Zazubovich, S. Photoluminescence of Cs$_4$PbBr$_6$ Crystals and Thin Films. *Chem. Phys.*

Lett. **1999**, *306*, 280–284.

(52)   Babin, V.; Fabeni, P.; Mihokova, E.; Nikl, M.; Pazzi, G. P. Luminescence of Cs$_4$PbBr$_6$

Aggregates in As-Grown and in Annealed CsBr : Pb Single Crystals. *Phys. Status Solidi B*

Basic Res. **2000**, *205*, 205–214.

(53)   Weerd, C. De; Lin, J.; Gomez, L.; Fujiwara, Y.; Suenaga, K.; Gregorkiewicz, T.

Hybridization of Single Nanocrystals of Cs4PbBr6 and CsPbBr3. *J. Phys. Chem. C* **2017**,

121, 19490–19496.

(54)   Quan, L. N.; Quintero-Bermudez, R.; Voznyy, O.; Walters, G.; Jain, A.; Fan, J. Z.; Zheng,

X.; Yang, Z.; Sargent, E. H. Highly Emissive Green Perovskite Nanocrystals in a Solid

State Crystalline Matrix. *Adv. Mater.* **2017**, *29*, 1–6.

(55)   Chen, X.; Zhang, F.; Ge, Y.; Shi, L.; Huang, S.; Tang, J.; Lv, Z.; Zhang, L.; Zou, B.; Zhong, H. Centimeter-Sized Cs_4PbBr_6 Crystals with Embedded $CsPbBr_3$ Nanocrystals Showing Superior Photoluminescence: Nonstoichiometry Induced Transformation and Light-Emitting Applications. *Adv. Funct. Mater.* **2018**, *28*, 1–7.

(56)   Jung, Y.-K.; Calbo, J.; Park, J.-S.; Whalley, L. D.; Kim, S.; Walsh, A. Intrinsic Doping Limit and Defect-Assisted Luminescence in Cs_4PbBr_6. *ChemRxiv* **2019**. https://doi.org/10.26434/chemrxiv.7629467.v3

(57)   Kang, B.; Biswas, K. Exploring Polaronic, Excitonic Structures and Luminescence in $Cs_4PbBr_6/CsPbBr_3$. *J. Phys. Chem. Lett.* **2018**, *9*, 830–836.

(58)   Han, D.; Shi, H.; Ming, W.; Zhou, C.; Ma, B.; Saparov, B.; Ma, Y. Z.; Chen, S.; Du, M. H. Unraveling Luminescence Mechanisms in Zero-Dimensional Halide Perovskites. *J. Mater. Chem. C* **2018**, *6*, 6398–6405.

(59)   Riesen, N.; Lockrey, M.; Badek, K.; Riesen, H. On the Origins of the Green Luminescence in the "Zero-Dimensional Perovskite" Cs_4PbBr_6: Conclusive Results from Cathodoluminescence Imaging. *Nanoscale* **2019**, *11*, 4001–4007.

(60)   Binsma, J. J. M.; Giling, L. J.; Bloem, J. Luminescence of $CuInS_2$. *J. Lumin.* **1982**, *27*, 35–53.

(61)   Sebastian, M.; Peters, J. A.; Stoumpos, C. C.; Im, J.; Kostina, S. S.; Liu, Z.; Kanatzidis, M. G.; Freeman, A. J.; Wessels, B. W. Excitonic Emissions and Above-Band-Gap Luminescence in the Single-Crystal Perovskite Semiconductors $CsPbBr_3$ and $CsPbCl_3$. *Phys. Rev. B - Condens. Matter Mater. Phys.* **2015**, *92*, 1–9.

(62)   Huang, L. Y.; Lambrecht, W. R. L. Electronic Band Structure, Phonons, and Exciton

Binding Energies of Halide Perovskites $CsSnCl_3$, $CsSnBr_3$, and $CsSnI_3$. *Phys. Rev. B - Condens. Matter Mater. Phys.* **2013**, *88*, 1–12.

(63)   Dursun, I.; De Bastiani, M.; Turedi, B.; Alamer, B.; Shkurenko, A.; Yin, J.; El-Zohry, A. M.; Gereige, I.; AlSaggaf, A.; Mohammed, O. F.; et al. $CsPb_2Br_5$ Single Crystals: Synthesis and Characterization. *ChemSusChem* **2017**, *10*, 3746–3749.

(64)   Tong, G.; Li, H.; Li, D.; Zhu, Z.; Xu, E.; Li, G.; Yu, L.; Xu, J.; Jiang, Y. Dual-Phase $CsPbBr_3$–$CsPb_2Br_5$ Perovskite Thin Films via Vapor Deposition for High-Performance Rigid and Flexible Photodetectors. *Small* **2018**, *14*, 1–8.

(65)   Zhang, X.; Jin, Z.; Zhang, J.; Bai, D.; Bian, H.; Wang, K.; Sun, J.; Wang, Q.; Liu, S. F. All-Ambient Processed Binary $CsPbBr_3$-$CsPb_2Br_5$ Perovskites with Synergistic Enhancement for High-Efficiency Cs-Pb-Br-Based Solar Cells. *ACS Appl. Mater. Interfaces* **2018**, *10*, 7145–7154.
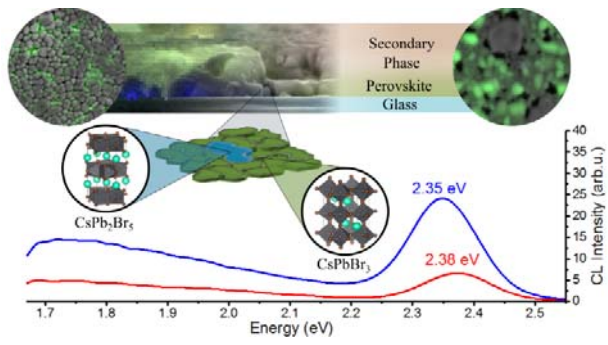
TOC Graphic: For table of contents only